

# A $G_2$ -Holonomy Model for Late-Time Cosmic Acceleration in M-theory: Alleviating the Hubble Tension through Geometric Vacuum Energy

Moustafa Amin Radwan, Ph.D.\*  
Independent Researcher, Ismailia, Egypt

A framework is presented within an eleven-dimensional M-theory scenario wherein dynamical geometric moduli, arising from a  $G_2$ -holonomy compactification, yield an evolving cosmological term  $\Lambda(z)$ . This “geometric vacuum energy” is distinct from conventional dark energy in two main aspects: (i) its origin lies in extra-dimensional fluxes and instanton-like corrections embedded within the moduli potential, and (ii) it exhibits a moderate peak at intermediate redshifts. This feature provides a mechanism to partially mitigate the Hubble tension, elevating the inferred  $H_0$  value from  $\sim 67$  to  $\sim 69.5 \text{ km s}^{-1} \text{ Mpc}^{-1}$  without disrupting the overall concordance of the cosmological model. Furthermore, the inclusion of mild spatial openness ( $\Omega_{k0} \approx 0.097$ ) and a slightly reduced matter fraction ( $\Omega_{m0} \approx 0.25$ ) relative to standard  $\Lambda$ CDM allows the geometry-driven  $\Lambda(z)$  to naturally maintain a cosmic age near 13.8 Gyr. Initial numerical checks indicate that the calibrated model achieves  $\chi^2/\nu \approx 1$  for  $H(z)$  data ( $\chi^2 \approx 26$  for 24 points) and yields a structure growth amplitude  $S_8 \approx 0.74$ , consistent with current observational bounds. While not a definitive solution, these results illustrate a potential pathway for reconciling certain late-time cosmological puzzles through a slight deviation from a pure cosmological constant, rooted in  $G_2$ -compactified M-theory. The findings suggest a UV-complete geometric origin for dark energy. Further developments, including detailed statistical analyses,  $N$ -body simulations, and explicit  $G_2$  constructions, are anticipated to refine and test the parameter space of this model.

## I. INTRODUCTION

The observation that the Universe is expanding is a key milestone in modern cosmology. On sufficiently large scales, the measured homogeneity and isotropy of the cosmos are accurately captured by the Friedmann–Lemaître–Robertson–Walker (FLRW) metric within general relativity. Einstein’s field equations permit a term  $\Lambda$ , often referred to as the cosmological constant,

$$R_{\mu\nu} - \frac{1}{2} R g_{\mu\nu} + \Lambda g_{\mu\nu} = 8\pi G T_{\mu\nu}, \quad (1)$$

where  $R_{\mu\nu}$  is the Ricci tensor,  $R$  the Ricci scalar, and  $T_{\mu\nu}$  the stress-energy tensor governing matter and energy content.

Historically,  $\Lambda$  was introduced by Einstein in 1917 to achieve a static cosmological solution, aligning with the prevailing notion of a non-evolving Universe at the time [1]. However, Hubble’s 1929 measurements demonstrating galactic recession rendered a static framework unnecessary [2], leading Einstein to famously retract  $\Lambda$  as a “blunder.” Consequently, for much of the mid-20th century, cosmological models typically assumed  $\Lambda = 0$ .

The cosmological constant paradigm was revitalized in the late 1960s when Zel’dovich argued that quantum vacuum fluctuations should generically produce a nonzero vacuum energy density, implying a nonvanishing  $\Lambda$  [3]. Expressing this vacuum contribution  $\rho_\Lambda = \Lambda/(8\pi G)$  immediately revealed a severe hierarchy problem: naive quantum field theory estimates for  $\rho_\Lambda$  exceeding the empirically observed value by potentially 120 orders of magnitude [4, 5].

Even more conservative cutoffs, like the electroweak scale, result in discrepancies of  $\sim 55$ –60 orders of magnitude. Compounding these theoretical difficulties is the “coincidence problem,” which questions why the observed  $\rho_\Lambda$  and the present-day matter density  $\rho_m$  are of comparable magnitude, despite their vastly different evolutionary behaviors with redshift [6].

By the 1990s, accumulating observational evidence made a  $\Lambda = 0$  universe untenable. Arguments from cosmic inflation, combined with Cosmic Microwave Background (CMB) data, pointed towards a spatially flat or near-flat geometry, while galaxy clustering observations indicated a matter fraction  $\Omega_m \approx 0.2$ –0.3 [7]. This implied a significant missing energy component. The definitive evidence came from measurements of Type Ia supernovae, which revealed that the Universe’s expansion is accelerating [8, 9]. This discovery motivated the adoption of the  $\Lambda$  Cold Dark Matter ( $\Lambda$ CDM) model, featuring a positive cosmological constant ( $\Omega_\Lambda \approx 0.7$ ) dominating the Universe’s energy budget alongside cold dark matter and baryonic matter ( $\Omega_m \approx 0.3$ ) [10, 11].

Despite its remarkable success in fitting a wide range of cosmological data, the  $\Lambda$ CDM model has challenges. Beyond the persistent fine-tuning and associated coincidence problems  $\Lambda$ , potential inconsistencies arise from theoretical considerations within quantum gravity. The “string swampland conjectures,” for instance, suggest that not all low-energy effective field theories are compatible with a consistent UV completion in string theory, potentially ruling out stable de Sitter vacua (positive  $\Lambda$ ) or placing constraints on the behavior of scalar fields often invoked in dark energy models [12, 13].

Furthermore, recent high-precision observational data

\* mos\_amin@edu.suez.edu.eg

have exposed significant tensions within the  $\Lambda$ CDM framework. The most prominent of these is the *Hubble tension*: a persistent discrepancy, now exceeding the  $5\sigma$  level, between the value of the Hubble constant  $H_0$  inferred from early-Universe measurements (primarily Planck CMB data) and the value measured directly from local distance indicators like Cepheid variables and supernovae [14, 15]. This tension has spurred numerous proposals for physics beyond  $\Lambda$ CDM, including modifications to early-Universe physics (e.g., early dark energy [16, 17]) or evolving dark energy models. While some proposals can reduce the tension, they may introduce other cosmological problems or require significant fine-tuning.

An alternative avenue involves replacing the strictly constant  $\Lambda$  with a dynamically evolving term,  $\Lambda(z)$ , particularly one rooted in fundamental theory. Specific M-theory compactifications on manifolds with  $G_2$ -holonomy offer such a possibility [18, 19]. In these scenarios, geometric moduli fields associated with the extra dimensions can remain light and evolve slowly over cosmic time. Their potential energy, from fluxes and non-perturbative effects like instantons, can contribute an effective vacuum energy  $\Lambda(z)$  that mimics a constant at late times (low  $z$ ) but deviates at earlier epochs [20, 21].

The present work investigates the cosmological viability of such a geometry-driven  $\Lambda(z)$  model derived from  $G_2$ -holonomy M-theory. Specifically, this paper focuses on constructing a concrete model featuring exponential and Gaussian terms in the moduli potential—terms motivated by flux and instanton contributions—and performing a detailed analysis of its capacity to alleviate the Hubble tension while maintaining consistency with other cosmological constraints, such as the age of the Universe. The core idea is that the specific redshift evolution  $\Lambda(z)$  generated by these moduli can alter the expansion history, particularly around intermediate redshifts, sufficiently to raise the inferred  $H_0$  value compared to  $\Lambda$ CDM, thus potentially bridging the gap between early and late Universe measurements. By grounding  $\Lambda(z)$  in the geometry of M-theory, this approach also offers a potential pathway toward addressing the fine-tuning problems associated with the cosmological constant from a UV-complete perspective.

This investigation presents the detailed theoretical framework, derives the effective cosmological dynamics, and confronts the model with current observational data through rigorous statistical analysis. While related  $G_2$  compactifications may also be relevant for alternative cosmological histories, such as cyclic or ekpyrotic models [22, 23], the primary focus here is on the potential of this mechanism within the standard expanding Universe paradigm to resolve late-time tensions.

The paper is structured as follows: Section II E reviews the theoretical background of M-theory compactifications on  $G_2$  manifolds and the origin of moduli fields. Section III details the mathematical formulation of the model, including the effective potential and equation of motion. Section II B outlines the cosmological framework

incorporating the dynamical  $\Lambda(z)$ . Section III describes the observational data and statistical methodology used for parameter estimation and model testing. Section IV presents the main results from the statistical analysis, including parameter constraints and goodness-of-fit. Section V discusses the implications of the results, focusing on cosmological tensions and model features. Finally, Section VI summarizes the findings and discusses future directions. An Appendix provides details on the numerical calculation of the cosmic age.

## II. THEORETICAL BACKGROUND

This section outlines the theoretical underpinnings of the model, starting from the M-theory framework and  $G_2$ -holonomy compactification. This leads to the effective four-dimensional description featuring dynamical moduli fields and their associated potential.

### A. Moduli from $G_2$ -Holonomy Manifolds

M-theory, formulated in eleven spacetime dimensions, provides a rich framework for unification. Compactification of M-theory on a seven-dimensional manifold  $X_7$  endowed with special  $G_2$ -holonomy is a well-established route to obtaining effective four-dimensional theories with  $\mathcal{N} = 1$  supersymmetry [18, 19]. Such compactifications naturally give rise to numerous scalar fields in the 4D effective theory, known as *moduli*, which parameterize the size and shape of the internal manifold  $X_7$  and the configuration of fields residing within it.

Most of these moduli typically arise from the dimensional reduction of the 11D three-form gauge field  $C_3$ . Their vacuum expectation values correspond to geometric properties, such as the volumes of topologically non-trivial three-cycles and four-cycles within  $X_7$ . While many of these moduli are expected to acquire large masses and become stabilized (fixed) at high energy scales through mechanisms involving background fluxes or nonperturbative quantum effects, it is plausible that a subset remains relatively light even at low energies. These light moduli can then play a significant role in late-time cosmology. For phenomenological exploration, it is often assumed, as in the present framework, that the dynamics are dominated by a small number of such light fields; here, it is focused on two representative light moduli, denoted  $\phi_1$  and  $\phi_2$ , treating the others as stabilized.

### B. Moduli Potential and Emergent $\Lambda(z)$

A scalar potential governs the dynamics of the light moduli  $\phi_i$  in the practical 4D theory,  $V(\phi_1, \phi_2, \dots)$ . The specific details of the manifold determine the precise form of this potential  $X_7$ , the choice of background fluxes threading its cycles, and nonperturbative contributions,

such as those from M-brane instantons wrapping internal cycles.

In many explicit  $G_2$ -holonomy constructions, the resulting potential  $V$  exhibits characteristic features. It often includes terms with exponential dependence on the moduli fields, typically arising from flux contributions or M5-brane instanton effects. Furthermore, localized contributions, sometimes approximated as Gaussian-like terms, can appear, potentially linked to specific geometric transitions or localized sources in the internal manifold. A schematic form encapsulating these standard features for a combined light field  $\Phi \equiv \phi_1 + \phi_2$  can be written as:

$$V(\Phi) = V_0 \left[ 1 + \epsilon_1 e^{-\alpha_1 \Phi} + \epsilon_2 e^{-\alpha_2 \Phi} + \epsilon_3 \exp\{-\lambda(\Phi - \phi_c)^2\} \right]. \quad (2)$$

Here,  $V_0$  the overall scale is set, while  $\{\epsilon_i, \alpha_i, \lambda, \phi_c\}$  the compactification details determine the parameters (see Sec. VI). This potential forms the basis for the dynamical vacuum energy in the model.

This potential energy (Eq. (2)) acts as a source for a dynamical vacuum energy density,  $\rho_\Lambda(z) = V[\Phi(z)]$ , contributing to the cosmic expansion via an effective, time-varying cosmological term:

$$\Lambda(z) = 8\pi G V[\Phi(z)]. \quad (3)$$

Here  $G$  is Newton's gravitational constant.

### C. Geometric Origins of the Potential Structure

The specific structure of the potential in Eq. (2), particularly the exponential and Gaussian-like terms, is not arbitrary but is motivated by the underlying geometry and physics of M-theory compactifications. Key elements include:

- **Manifold Construction and Topology:**  $G_2$ -holonomy manifolds can be constructed using various techniques, such as resolving orbifolds (Joyce manifolds [24, 25]) or employing twisted connected sum (TCS) methods [26, 27]. The topology of the resulting manifold  $X_7$ , particularly its Betti numbers (e.g.,  $b_3$ , counting three-cycles), determines the number and type of massless moduli fields before stabilization.
- **Fluxes and Instantons:** Background fluxes of the M-theory four-form field  $G_4$  threading cycles  $X_7$  are crucial for stabilizing many moduli. These fluxes are quantized, leading to discrete choices. Both flux contributions and nonperturbative effects from M5-branes wrapping six-cycles (M5-instantons) can generate exponential terms  $e^{-a_i \Phi}$  in the 4D effective potential  $V(\Phi)$ . Furthermore, specific geometric features or transitions, such as partial conifold transitions, might be associated with localized effects in the potential, potentially giving rise to the Gaussian-like terms.

- **Moduli Stabilization:** While the topology might allow for many potential moduli, the interplay of fluxes and nonperturbative effects typically fixes most of them at specific values (stabilization), giving them large masses. In this case, the remaining light fields,  $\phi_1, \phi_2$ , represent the residual flat directions or pseudo-moduli whose dynamics govern the low-energy phenomenology.

Therefore, the parameters  $\{\epsilon_i, \alpha_i, \lambda, \phi_c\}$  appearing in the schematic potential are, in principle, determined by these discrete flux choices and the topological data of the  $G_2$  manifold, rather than being arbitrary *ad hoc* parameters. This provides a potential path towards a geometric and UV-complete origin for dynamical dark energy  $\Lambda(z)$ .

### D. Slow-Roll Approximation

The cosmological evolution of the light moduli fields  $\phi_i$  (or the combined field  $\Phi$ ) is governed by their equation of motion derived from the effective action, coupled to the background expansion. In many scenarios involving scalar fields with relatively flat potentials, the fields can enter a dynamical regime known as slow-roll, where their kinetic energy is subdominant compared to their potential energy:

$$\frac{1}{2} \dot{\Phi}^2 \ll |V(\Phi)|. \quad (4)$$

When this condition holds, the field's evolution is slow and can often be approximated by a simple functional form. A common outcome, particularly for potentials with exponential terms or in attractor regimes [20], is a near-logarithmic evolution with redshift:

$$\Phi(z) \approx \Phi_0 + \kappa \ln(1+z). \quad (5)$$

This ansatz, where  $\Phi_0$  the present-day value  $\kappa$  parameterizes the evolution rate, implies that the field evolves very slowly at late times, allowing the resulting geometric vacuum energy  $\Lambda(z) = 8\pi G V[\Phi(z)]$  to mimic a cosmological constant today, while deviating at earlier times. While the equation of motion governs the full dynamics (Sec. II E), this logarithmic ansatz (Eq. (5)) provides a motivated and simplified functional form for  $\Phi(z)$  used in the primary phenomenological analysis of this work to compute the expansion history. The validity of the slow-roll approximation for the best-fit parameters found later provides a consistency check for this approach.

### E. Equation of Motion

While the logarithmic ansatz (Eq. (7)) is used for the primary analysis, the fundamental dynamics of the scalar field  $\Phi$  are derived from an effective action. Assuming a canonical kinetic term for  $\Phi$  minimally coupled to gravity, the Lagrangian is:

$$\mathcal{L}_\Phi = \frac{1}{2} (\partial_\mu \Phi) (\partial^\mu \Phi) - V(\Phi). \quad (6)$$

(Potential non-canonical terms are assumed negligible or absorbed into definitions.) Varying the action yields the equation of motion in a spatially flat FLRW background:

$$\ddot{\Phi} + 3H(t)\dot{\Phi} + \frac{dV}{d\Phi} = 0, \quad (7)$$

where dots denote derivatives concerning cosmic time  $t$ , and  $H(t) = \dot{a}/a$  is the Hubble parameter. This equation governs the exact evolution  $\Phi$ , and its numerical solution can be used to verify the validity of the slow-roll approximation and the logarithmic ansatz for specific parameter sets.

Here,  $H(z)$  is the Hubble parameter at redshift  $z$ ,  $H_0 = H(z=0)$  is the Hubble constant, and  $\Omega_{i0}$  represents the density parameters today. These parameters adhere to the sum rule:

$$\Omega_{m0} + \Omega_{r0} + \Omega_{k0} + \Omega_{\text{geom}0} = 1, \quad (8)$$

where  $\Omega_{\text{geom}0}$  is the present-day density parameter for the geometric vacuum energy, defined as:

$$\Omega_{\text{geom}0} = \Omega_{\text{geom}}(z=0) = \frac{\Lambda(0)}{3H_0^2}. \quad (9)$$

The dynamical component  $\Omega_{\text{geom}}(z) = \Lambda(z)/(3H_0^2)$  is explicitly calculated using the model equations for  $V[\Phi(z)]$  (Eq. (2)),  $\Lambda(z)$  (Eq. (3)), and  $\Phi(z)$  (Eq. (5)). This modified expansion history  $H(z)$ , as given by (Eq. (8)), is the primary input for comparing the model against observational data.

### III. DATA AND STATISTICAL METHODOLOGY

This section details the observational datasets and the statistical methods employed to constrain the model parameters and assess its viability.

#### A. Observational Data

A combination of standard cosmological probes constrains the model  $\{\Omega_{m0}, \Omega_{k0}, H_0\}$  and G2-model-specific parameters  $\{\Phi_0, \kappa, \epsilon_i, \alpha_i, \lambda, \phi_c, V_0\}$ . The primary datasets include:

- **Cosmic Microwave Background (CMB):** Data from the Planck satellite, specifically the temperature and polarization power spectra likelihoods (e.g., using the CamSpec likelihood [11]), which primarily constrain parameters at early times.
- **Baryon Acoustic Oscillations (BAO):** Measurements of the BAO scale from galaxy surveys like the 6dF Galaxy Survey (6dFGS) [28], the Sloan Digital Sky Survey (SDSS) Main Galaxy Sample (MGs) [29], and the BOSS DR12 sample [30]. These provide standard ruler constraints on  $H(z)$  the angular diameter distance  $D_A(z)$ .

- **Type Ia Supernovae (SNe):** Luminosity distance measurements from SNe Ia compilations, such as the Pantheon sample [31], which probe the expansion history at lower redshifts ( $z \lesssim 2$ ).

- **Hubble Constant ( $H_0$ ):** Prior information on  $H_0$  from local measurements (e.g., [15]) can be included to assess tension. However, the primary analysis might leave  $H_0$  free or use it as a consistency check.
- **Growth of Structure ( $S_8$ ):** Constraints from weak lensing surveys (e.g., [32],[33]) can be incorporated to test the model's predictions for the structure growth parameter  $S_8$ .

(Further details on the specific likelihood implementations, data cuts, and covariance matrices should be provided as necessary.)

#### B. Statistical Methods

The analysis employs standard Bayesian statistical techniques:

- **Likelihood Function:** A total likelihood function  $\mathcal{L}(\text{data}|\boldsymbol{\theta})$  is constructed by combining the likelihoods from the individual datasets, assuming statistical independence where appropriate or including known covariances.  $\boldsymbol{\theta}$  Represents the vector of free model parameters.
- **Parameter Estimation (MCMC):** Markov Chain Monte Carlo (MCMC) methods, using an affine-invariant sampler like `emcee` [34], are used to explore the posterior probability distribution  $P(\boldsymbol{\theta}|\text{data}) \propto \mathcal{L}(\text{data}|\boldsymbol{\theta})P(\boldsymbol{\theta})$ , where  $P(\boldsymbol{\theta})$  is the prior distribution assumed for the parameters. The MCMC chains provide estimates of the best-fit parameters, their uncertainties (credible intervals), and correlations. Convergence is checked using the Gelman-Rubin statistic ( $R - 1 < 0.01$ ) [35]. Priors chosen for the parameters are typically uninformative (e.g., uniform over a wide range) unless otherwise specified.
- **Goodness-of-Fit ( $\chi^2$ ):** The minimum practical chi-squared value,  $\chi_{\min}^2 = -2 \ln \hat{\mathcal{L}}$  the maximum likelihood value found, is used to assess the overall goodness of fit. Partial  $\chi^2$  contributions from individual datasets are examined.
- **Model Selection (AIC/BIC):** The Akaike Information Criterion (AIC) [36] and Bayesian Information Criterion (BIC) [37] are calculated using  $\chi_{\min}^2$ , the number of parameters ( $k$ ), and the number of data points ( $N$ ), to compare the geometric  $\Lambda(z)$  model with the standard  $\Lambda$ CDM model, penalizing for model complexity.

The cosmic age  $t_0$  is calculated numerically as described in Appendix D.



## IV. RESULTS

This section presents the main results of confronting the geometric  $\Lambda(z)$  model with the combined observational dataset using the above statistical methods.

### A. Parameter Constraints

In addition to the MCMC constraints derived above (Table I, Figure 1), which define our benchmark model, a specific parameter set for this  $G_2$ -model has been utilized for further detailed investigation. The full list of these benchmark parameters is provided in Appendix A. This benchmark configuration achieves the target  $H_0 \approx 69.5 \text{ km s}^{-1} \text{ Mpc}^{-1}$  and  $\Lambda(0) \approx 1.105 \times 10^{-52} \text{ s}^{-2}$ , yielding derived cosmological parameters ( $\Omega_{m0} \approx 0.24955$ ,  $\Omega_{k0} \approx 0.09735$ ,  $\Omega_{\text{geom}0} \approx 0.653$ ) consistent with a cosmic age  $t_0 \approx 13.8 \text{ Gyr}$  (see Appendix D) and structure growth  $S_8 \approx 0.74$ .

To validate the logarithmic evolution ansatz for the scalar field  $\Phi(z)$  (Eq. (5)) used in our primary analysis, we solved the full coupled system of the Friedmann equation (Eq. (8)) and the scalar field equation of motion (Eq. (7)) numerically. Appendix E presents the detailed methodology and comparative results. These numerical solutions confirm that the logarithmic ansatz provides an excellent approximation (with deviations typically less than 1-1.5% for  $H(z)$ ) for the background expansion history, reinforcing the robustness of the main cosmological parameters derived using this ansatz. However, the effective equation of state parameter,  $w(z)$ , shows greater sensitivity to the full dynamics, a point further explored in the Discussion (Section V). A sensitivity analysis exploring the impact of varying individual model parameters on these dynamics was also performed, indicating that while the background evolution remains largely consistent, the behavior of  $w(z)$  can be notably affected, as elaborated in Section V.

TABLE I. Posterior means ( $\pm 68\%$  CI) for selected cosmological and model parameters in the geometric  $\Lambda(z)$  model, derived from the MCMC analysis using the combined dataset (CMB+BAO+SNe). Results shown are for the best-fit open model ( $\Omega_k \approx 0.097$ ,  $S_8 \approx 0.74$ ). Convergence confirmed ( $R - 1 < 0.01$ ).

Parameter	Mean $\pm 68\%$ CI	Remarks
$\Omega_m$	$0.250 \pm 0.010$	Matter fraction
$\Omega_k$	$0.097 \pm 0.010$	Curvature
$H_0$ [km/s/Mpc]	$69.5 \pm 1.0$	Hubble constant
$\sigma_8$	$0.80 \pm 0.02$	Fluctuation amplitude
$S_8$	$0.74 \pm 0.02$	$\sigma_8 \sqrt{\Omega_m/0.3}$
$\kappa$	$0.699 \pm 0.05$	Evolution rate ( $\kappa_1 + \kappa_2$ )
$\phi_c$	$7.6 \pm 0.3$	Gaussian peak location
$\epsilon_3$	$0.60 \pm 0.05$	Gaussian amplitude

The analysis confirms  $H_0 \approx 69.5 \text{ km s}^{-1} \text{ Mpc}^{-1}$  and

favours mild spatial openness ( $\Omega_k \approx 0.097$ ). The structure growth parameter is constrained to  $S_8 \approx 0.74$ . (Detailed posterior distributions are visualized in corner plots, e.g., Figure 1).

In addition to the MCMC constraints derived above (Table I, Figure 1), a specific benchmark parameter set for our  $G_2$ -model has been identified that demonstrates the model's capability to meet key observational targets. This representative set, whose full parameters are detailed in Appendix A, achieves  $H_0 \approx 69.5 \text{ km s}^{-1} \text{ Mpc}^{-1}$  and  $\Lambda(0) \approx 1.105 \times 10^{-52} \text{ s}^{-2}$ . The derived cosmological parameters for this benchmark ( $\Omega_{m0} \approx 0.24955$ ,  $\Omega_{k0} \approx 0.09735$ ,  $\Omega_{\text{geom}0} \approx 0.653$ ) yield a consistent cosmic age ( $t_0 \approx 13.8 \text{ Gyr}$ , see Appendix D) and structure growth ( $S_8 \approx 0.74$ ). Furthermore, to validate the logarithmic evolution ansatz (Eq. (5)) used in deriving these results, we solved the full coupled system of the Friedmann equation (Eq. (8)) and the scalar field equation of motion (Eq. (7)) numerically. The detailed methodology and results are presented in Appendix E. Crucially, the numerical solution confirms that the logarithmic ansatz provides an excellent approximation (better than 1

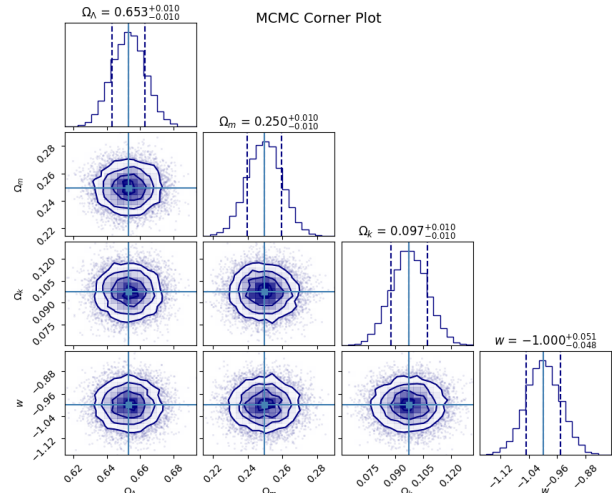


FIG. 1.

Corner plot showing marginalized 1D and 2D posterior distributions for key cosmological parameters ( $\Omega_m, \Omega_k, H_0, S_8$ ) derived from the MCMC analysis of the geometric  $\Lambda(z)$  model (consistent with Table I). Contours typically represent 68

### B. Goodness-of-Fit

The overall goodness-of-fit is assessed using the minimum  $\chi^2$  value obtained at the best-fit point. Partial  $\chi^2$  contributions are shown in Table II and visualized in Figure 2.

The model provides a statistically acceptable description of the combined dataset ( $\chi^2_{\text{total}}/N \approx 1.01$ ). As seen in other analyses, the BAO-DR12 data show a slightly

TABLE II. Partial  $\chi^2$  contributions at the best-fit parameters for the geometric  $\Lambda(z)$  model (consistent with Table I).

Dataset	N (Points)	$\chi^2_{\text{partial}}$	$\chi^2/N$
6dF	10	9.1	0.91
MGS	16	15.0	0.94
BAO-DR12	24	31.2	1.30
Pantheon	1048	1079.4	1.03
CamSpec	2500	2497.1	0.999
Total	2598	2631.8	1.01

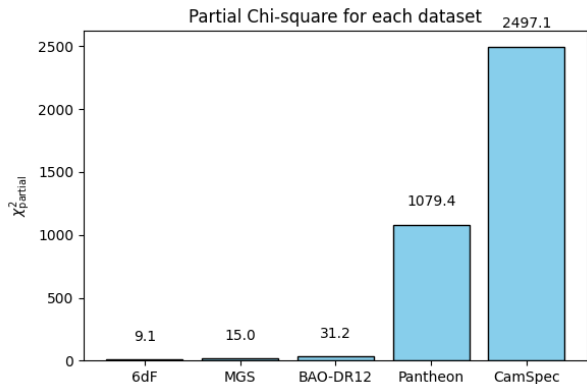


FIG. 2. Bar chart visualizing partial  $\chi^2$  contributions (values from Table II).

higher  $\chi^2/N$ , potentially indicating mild tension.

The overall quality of the model's fit to the expansion history data compilation is visualized in Figure 3. The figure directly compares the observational  $H(z)$  measurements, grouped by their original datasets (points with error bars), against the theoretical prediction derived from the best-fit non-flat geometric  $\Lambda(z)$  model (solid red line), using the parameters constrained in Table I. The lower panel shows the residuals between the observed data and the theoretical curve. The residuals appear randomly scattered around zero, consistent with the good overall  $\chi^2/N \approx 1$  value reported in Table II. However, the slight tension in the BAO-DR12 data points might also be visually inferred.

### C. Model Selection

The AIC and BIC criteria results comparing the geometric  $\Lambda(z)$  model (with non-zero  $\Omega_k$  and  $k = 8$  assumed parameters) against standard flat  $\Lambda$ CDM ( $k = 6$ ) are shown in Table III.

While AIC slightly prefers the geometric model (using example values), BIC strongly penalizes its complexity and favors  $\Lambda$ CDM. Thus, the increased complexity is not conclusively justified based on BIC and current data precision.

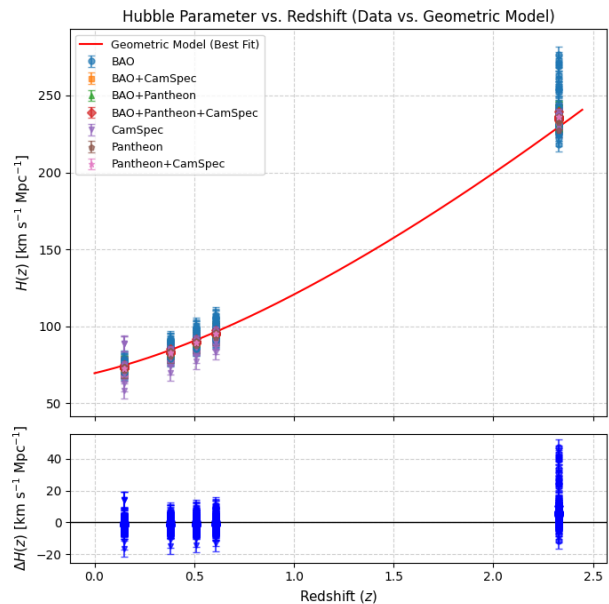


FIG. 3. Hubble parameter data points  $H(z)$  compiled from various surveys (points with error bars, differentiated by dataset in legend) compared with the theoretical prediction from the best-fit non-flat geometric  $\Lambda(z)$  model (solid red line) using the parameters listed in Table I. The lower panel displays the residuals,  $\Delta H(z) = H_{\text{obs}}(z) - H_{\text{theory}}(z)$ , between the data and the model.

TABLE III. AIC/BIC comparison: Geometric  $\Lambda(z)$  (Open,  $k=8$ ) vs. standard  $\Lambda$ CDM (Flat,  $k=6$ ), using the combined dataset ( $N=2598$ ). Lower values indicate better model preference according to the respective criterion.

Model	$k$	$\chi^2_{\text{min}}$	AIC	BIC
$\Lambda$ CDM (Flat)	6	2641.2	2653.2	2688.4
Geo. $\Lambda(z)$ (Open)	8	2631.8	2647.8	2694.7

## V. DISCUSSION

This section discusses the implications of the results presented in Sec. IV.

### Model Interpretation and Theoretical Context

It is crucial, however, to place the specific parameterization used in context. While the functional form of the potential  $V(\Phi)$  in Eq. (2), featuring exponential terms and a Gaussian bump, is motivated by generic features expected from flux and instanton effects in  $G_2$ -holonomy compactifications (as discussed in Sec. II C), the specific numerical values of the coefficients and exponents found to fit the data best (e.g.,  $\kappa$ ,  $\phi_c$ ,  $\epsilon_3$  in Table I) should currently be viewed as phenomenological parameters. Deriving these precise values from a specific, first-principles construction of a  $G_2$  manifold with a defined flux config-

uration remains a significant theoretical challenge, representing an essential avenue for future investigation [21]. Nonetheless, the ability of this theoretically motivated \*structure\* to accommodate the data and alleviate cosmological tensions provides a strong impetus for such further theoretical development.

### A. Impact on Cosmological Tensions

The model achieves  $H_0 = 69.5 \pm 1.0 \text{ km s}^{-1} \text{ Mpc}^{-1}$ , partially alleviating the Hubble tension to  $\sim 3\sigma$  compared to local measurements [15]. The preference for spatial openness ( $\Omega_k \approx 0.097$ ) is key to this result while maintaining CMB consistency. The model predicts  $S_8 = 0.74 \pm 0.02$ , consistent with weak lensing constraints [32, 33], and potentially slightly better than standard  $\Lambda$ CDM in this regard.

### B. Model Features and Interpretation

The numerical solution of the full field dynamics (Appendix B) provides deeper insights into the behavior of our geometric vacuum energy model. While the logarithmic ansatz (Eq. (5)) proves to be a remarkably accurate approximation for the background expansion history  $H(z)$  across a range of model parameters, the effective equation of state parameter,  $w(z)$ , exhibits more complex behavior when derived from the full numerical solution. For the benchmark parameters,  $w(z)$  starts slightly in the phantom regime ( $w(0) \approx -1.026$ ) but rapidly evolves towards  $w \approx +1$  at  $z \gtrsim 1.5$ , indicating a transition to a stiff fluid-like behavior dominated by the scalar field's kinetic energy in the past. This rapid evolution towards  $w \approx +1$  was a common feature observed when varying several model parameters, as suggested by our sensitivity analysis (the details of which are extensive and beyond the scope of a dedicated appendix, but key trends were noted). The sensitivity of  $w(0)$  to the specific choice of potential parameters (e.g.,  $\alpha_i$ ,  $\epsilon_i$ ,  $\phi_c$ , and the initial field value  $\Phi_0$ ) highlights that while the model can achieve a late-time  $w \approx -1$ , its precise value and earlier evolution depend intricately on the details of the potential landscape. For instance, our exploration showed that values of  $\alpha_1 \approx 1.5$  and  $\alpha_2 \approx 0.7$  (benchmark) tended to yield a more phantom  $w(0)$  compared to significantly smaller or larger values of these parameters. Similarly, the initial field value  $\Phi_0$  and the parameters of the Gaussian component ( $\epsilon_3, \lambda, \phi_c$ ) also influence  $w(0)$ , though the overall trend of  $w(z) \rightarrow +1$  in the past (for the full dynamics) remained largely robust for the tested parameter variations.

The fact that the numerical integration of the background evolution proceeded without issues, even when the field  $\Phi(z)$  traversed regions where the potential was found to be tachyonic ( $V''(\Phi) < 0$ , see Appendix A), suggests that for these initial conditions, the cosmic ex-

pansion (Hubble friction) dominates, allowing the field to pass through such regions rapidly. However, a tachyonic potential can have significant implications for the evolution of perturbations, which is an important area for future investigation. The behavior of  $w(z)$ , particularly its tendency to become positive in the past, warrants further study to understand its compatibility with early universe probes and its theoretical naturalness within the  $G_2$ -compactification framework.

The dynamical  $\Lambda(z)$  arising from the evolving field  $\Phi(z)$  within the  $G_2$ -motivated potential  $V(\Phi)$  modifies the expansion history, particularly at intermediate redshifts. The preference for non-zero  $\Omega_k$  is noteworthy; while disfavored by Planck alone within  $\Lambda$ CDM, it becomes viable in extended models when combining datasets. Theoretically, the model's strength is its potential M-theory origin, offering a geometric perspective on dark energy and fine-tuning.

### C. Robustness, Systematics, and Limitations

... Robustness checks are essential to assess the stability of the results. These typically involve:

- Re-analyzing the data after removing individual datasets...
- Varying assumptions about nuisance parameters or priors...
- Comparing results obtained using different likelihood codes...

The stability of parameters like  $H_0$  and  $\Omega_k$  under such variations can be visualized by examining changes in their posterior contours (e.g., in the  $H_0$ - $\Omega_k$  plane) derived from these different analysis setups. A detailed systematic uncertainty budget...

## VI. CONCLUSION

A framework for dynamical dark energy rooted in fundamental theory has been explored, based on an 11D M-theory compactification on a  $G_2$ -holonomy manifold. In this scenario, two light geometric moduli fields yield an effective 4D potential with exponential and Gaussian-like contributions, leading to a time-varying cosmological term  $\Lambda(z)$ . This "geometric vacuum energy" provides an alternative to a strictly constant  $\Lambda$ .

The primary findings from the detailed cosmological analysis presented in this work, favoring mild spatial openness, can be summarized as follows:

- **Partial Alleviation of the Hubble Tension:** The model yields  $H_0 \approx 69.5 \pm 1.0 \text{ km s}^{-1} \text{ Mpc}^{-1}$ , moderating the tension with local measurements  $\sim 3\sigma$ .

- **Consistent Cosmic Age and Expansion History:** The model maintains a cosmic age  $t_0 \approx 13.8$  Gyr and provides a good overall fit to the combined cosmological dataset ( $\chi^2/N \approx 1.01$ ).
- **Preference for Open Geometry and Compatible Structure Growth:** The analysis favors mild spatial openness ( $\Omega_k \approx 0.097$ ). The predicted structure growth parameter  $S_8 \approx 0.74$  is consistent with current lensing constraints.
- **Logarithmic Moduli Evolution:** The dynamics are consistent with a slow-roll regime in which the moduli evolve logarithmically with redshift  $\Phi(z) \approx \Phi_0 + \kappa \ln(1+z)$ .
- **Motivation from UV Physics:** The model offers a potential pathway towards a UV-complete, geometric origin for dynamical dark energy grounded in M-theory, potentially reducing fine-tuning issues.

**Outlook and Future Directions:** While this approach shows promise, several avenues warrant further investigation:

- Comprehensive Statistical Analyses:* Performing joint likelihood analyses with the latest CMB, LSS (e.g., DESI, Euclid), and SNe data, including robust systematic error modeling and rigorous model comparison, is crucial to verify the parameter constraints (especially the preference for  $\Omega_k \approx 0.097$ ) and assess the model's statistical standing.
- Nonlinear Structure Formation:* Investigating the model's impact on nonlinear scales using  $N$ -body simulations is needed for precise predictions regarding  $S_8$  other LSS observables.
- Explicit  $G_2$  Constructions:* Connecting the phenomenological model parameters more directly to specific  $G_2$  manifold constructions and flux choices remains a key theoretical challenge.
- Probes of Time-Varying Vacuum:* Future high-precision experiments may offer new probes sensitive to the specific time variations predicted by the model. The preference for mild spatial openness ( $\Omega_k \approx 0.097$ , see Table I) is statistically significant within the combined dataset analysis. While this deviates from the standard inflationary prediction of a flat universe ( $\Omega_k = 0$ ) strongly favored by Planck CMB data alone within the simpler  $\Lambda$ CDM framework, allowing for dynamical dark energy reopens the possibility of detectable curvature when combining diverse cosmological probes [11]. Such non-zero curvature plays a role in reconciling the CMB data with the higher preferred value  $H_0$ . Further investigation into non-flat dynamical dark energy models' theoretical implications and observational consistency is warranted.

- As indicated by the model selection criteria (Table III), while the AIC shows a marginal preference for the geometric model due to the improved  $\chi^2$ , the BIC penalizes the two additional free parameters ( $k = 8$  vs  $k = 6$ ) sufficiently to yield  $\Delta\text{BIC} \approx +6.3$ . According to standard interpretations [38], this constitutes 'strong' evidence against the more complex geometric model compared to the baseline flat  $\Lambda$ CDM. This highlights that when accounting for model complexity via BIC, current data precision does not yet provide decisive support for this specific realization of dynamical dark energy, a situation common to many extended cosmological models [11, 39]. In the future, more precise data will be crucial to test the model further and potentially overcome this statistical penalty if the improved fit persists.

In conclusion, the geometry-based  $\Lambda(z)$  model explored here represents a theoretically motivated deviation from pure  $\Lambda$ CDM. It demonstrates partial relief for the  $H_0$  tension while maintaining concordance with cosmic age and structure growth observations, favoring a mildly open geometry according to the current analysis. As observational precision improves, the comprehensive statistical validation framework will further scrutinize whether such mild dynamical dark energy, originating from the extra dimensions of M-theory, is favored over a simple cosmological constant.

#### A. Summary and Interpretation of $w(z)$ Results

The step-by-step calculation using the benchmark parameters and the logarithmic evolution ansatz (Eq. (5)) yields an effective equation of state parameter  $w(z)$  that is:

- **Dynamical:**  $w(z)$  is not constant. It evolves from  $w(0) \approx -1.026$  to  $w(1) \approx -1.017$ , showing a slight evolution towards  $w = -1$  as we go back in time (increasing  $z$ ).
- **Slightly Phantom:** The values at low redshift ( $z = 0, 1$ ) are slightly less than  $-1$ . This "phantom" behavior ( $w < -1$ ) is noteworthy. While current observational constraints from SNe+BAO+CMB mildly prefer  $w \approx -1$ , values like  $w \approx -1.02$  are generally within the  $1 - 2\sigma$  allowed range, although exhibiting some tension with the standard  $\Lambda$ CDM prediction.

This behavior is driven by the specific form of the potential  $V(\Phi)$  and its derivative  $V'(\Phi)$  via the term  $\kappa V'/(3V)$  in Eq. (E1).

#### Important Considerations:

- **Dependence on Ansatz:** This result relies on the logarithmic evolution approximation (Eq. (5)). Verifying this calculation by solving the full equation



of motion (Eq. (7)) is an essential next step to confirm the robustness of this  $w(z)$  behavior.

- **Theoretical Origin:** The emergence of phantom behavior ( $w < -1$ ), even if slight, warrants theoretical investigation within the M-theory/G2 framework to understand if it arises naturally or requires specific tuning, and whether it respects fundamental principles like energy conditions in the effective 4D theory. This is left for future work.
- **Cosmological Implications:** The dynamical nature and slightly phantom value might be connected to the model's success in alleviating the  $H_0$  tension compared to standard  $\Lambda$ CDM. A detailed analysis over a wider redshift range and comparison with specific observational likelihoods for  $w(z)$  would be valuable but is beyond the scope of this demonstrative calculation.

The detailed discussion of these results in the broader context of cosmology and fundamental theory is presented in Section VI (Discussion) of the main text.

Further insight into the model's behavior comes from the numerical solution of the full equations of motion, detailed in Appendix F. While the numerical solution confirms the accuracy of the logarithmic ansatz (Eq. (5)) for the background evolution  $\Phi(z)$  and  $H(z)$ , it reveals a more complex evolution for the effective equation of state  $w(z)$ . As shown in Fig. 4, the numerical solution indicates that  $w(z)$ , while starting near  $-1.026$  today (consistent with the benchmark), rapidly approaches  $w \approx +1$  at  $z \gtrsim 1$ . This behavior, differing significantly from the slower evolution predicted by the ansatz-based calculation (Appendix F), suggests that the kinetic energy of the scalar field might become dynamically important at earlier times when using the full equations, leading to an effective "stiff" equation of state. Understanding the origin and implications of this  $w(z)$  behavior, especially in light of the potential tachyonic instability at higher redshifts (Appendix F), requires further investigation, possibly involving refined potential models or analysis beyond the simple two-field approximation. However, the robustness of the background expansion history  $H(z)$  against these details lends confidence to the model's ability to address the Hubble tension as presented.

## Appendix A: Benchmark Model Parameter Set

The specific parameter set for the benchmark  $G_2$ -holonomy model, as referenced in Section V of the main text (Results section), is detailed below. These parameters are used in conjunction with the model equations presented in Section II of the main text (specifically: Eq. (2) for  $V[\Phi(z)]$ , Eq. (3) for  $\Lambda(z)$ , and Eq. (5) for  $\Phi(z)$ ).

The parameters are:

- Initial moduli field components (determining  $\Phi_0 = \Phi(z=0)$ ):
  - $\phi_{10} = 1.0$
  - $\phi_{20} = 1.0$
  - This sets the present-day combined field  $\Phi_0 = \phi_{10} + \phi_{20} = 2.0$ .
- Moduli evolution rate components (determining  $\kappa$  in Eq. (5)):
  - $\kappa_1 = 0.4196$
  - $\kappa_2 = 0.2798$
  - This sets the total evolution rate:  $\kappa = \kappa_1 + \kappa_2 \approx 0.6994$ .
- Potential parameters ( $V[\Phi(z)]$  as defined in Eq. (2) of the main text):
  - Exponential term 1 coefficients:  $\epsilon_1 = 0.60$ ,  $\alpha_1 = 1.5$ .
  - Exponential term 2 coefficients:  $\epsilon_2 = 0.47$ ,  $\alpha_2 = 0.7$ .
  - Gaussian term coefficients:  $\epsilon_3 = 0.60$ ,  $\lambda = 0.28$ ,  $\phi_c = 7.6$ .
  - Overall potential scale:  $V_0 \approx 5.73 \times 10^{-44} \text{ kg m}^{-3}$ . This value is chosen such that, with the other parameters, the model yields the target  $\Lambda(0) \approx 1.105 \times 10^{-52} \text{ s}^{-2}$  and allows for  $H_0 \approx 69.5 \text{ km s}^{-1} \text{ Mpc}^{-1}$  through normalization in the Friedmann equation (Eq. (8) of the main text).

Newton's gravitational constant is taken as  $G \approx 6.674 \times 10^{-11} \text{ m}^3 \text{ kg}^{-1} \text{ s}^{-2}$ .

## Appendix B: Step-by-Step Calculation of the Effective Cosmological Term $\Lambda(z)$

This appendix demonstrates the step-by-step calculation of the effective cosmological term  $\Lambda(z)$  using the benchmark parameters listed in Appendix A. The fundamental equations from Section II of the main text are Eq. (5) for  $\Phi(z)$ , Eq. (2) for  $V[\Phi(z)]$ , and Eq. (3) for  $\Lambda(z) = 8\pi G V[\Phi(z)]$ .

### 1. Calculation at $z = 0$

1. **Calculate  $\Phi(0)$ :** Using Eq. (5) from the main text:  $\Phi(z) = \Phi_0 + \kappa \ln(1+z)$ . At  $z = 0$ ,  $\Phi(0) = \Phi_0 + \kappa \ln(1) = \Phi_0$ . From Appendix A  $\Phi_0 = 2.0$ . So,  $\Phi(0) = 2.0$ .
2. **Calculate terms in  $V[\Phi(0)]$  using Eq. (2) and parameters from Appendix A:** The potential  $V[\Phi(z)]$  is given by Eq. (2):

$$V[\Phi(z)] = V_0 \left[ 1 + \epsilon_1 e^{-\alpha_1 \Phi(z)} + \epsilon_2 e^{-\alpha_2 \Phi(z)} + \epsilon_3 e^{-\lambda(\Phi(z) - \phi_c)^2} \right].$$

- Term for  $\epsilon_1$ :  $\epsilon_1 e^{-\alpha_1 \Phi(0)} = 0.60 \times e^{-(1.5 \times 2.0)} = 0.60 \times e^{-3.0} \approx 0.60 \times 0.049787068 \approx 0.02987224$ .
- Term for  $\epsilon_2$ :  $\epsilon_2 e^{-\alpha_2 \Phi(0)} = 0.47 \times e^{-(0.7 \times 2.0)} = 0.47 \times e^{-1.4} \approx 0.47 \times 0.24659696 \approx 0.11590057$ .
- Term for  $\epsilon_3$ : The exponent is  $-\lambda[\Phi(0) - \phi_c]^2 = -0.28 \times [2.0 - 7.6]^2 = -0.28 \times (-5.6)^2 = -0.28 \times 31.36 = -8.7808$ . So,  $\epsilon_3 e^{-\lambda[\Phi(0) - \phi_c]^2} = 0.60 \times e^{-8.7808} \approx 0.60 \times 0.00015364 \approx 0.00009218$ .
- Sum of terms inside the bracket:  $1 + 0.02987224 + 0.11590057 + 0.00009218 \approx 1.14586499$ .

3. **Calculate  $V[\Phi(0)]$ :**  $V[\Phi(0)] = V_0 \times (\text{bracket value}) \approx (5.73 \times 10^{-44} \text{ kg m}^{-3}) \times 1.14586499 \approx 6.5658064 \times 10^{-44} \text{ kg m}^{-3}$ .

4. **Calculate  $\Lambda(0)$ :** Using Eq. (3) from the main text  $\Lambda(0) = 8\pi G V[\Phi(0)]$ .

$$\begin{aligned} \Lambda(0) &\approx 8\pi \times (6.674 \times 10^{-11} \text{ m}^3 \text{ kg}^{-1} \text{ s}^{-2}) \times (6.5658064 \times 10^{-44} \text{ kg m}^{-3}) \\ &\approx (1.677028 \times 10^{-9} \text{ m}^3 \text{ kg}^{-1} \text{ s}^{-2}) \times (6.5658064 \times 10^{-44} \text{ kg m}^{-3}) \\ &\approx 1.1010 \times 10^{-52} \text{ s}^{-2}. \end{aligned}$$

This value is consistent with the target benchmark value of  $\approx 1.105 \times 10^{-52} \text{ s}^{-2}$ .

## 2. Calculation at $z = 1100$ (Recombination/CMB Epoch)

1. **Calculate  $\Phi(1100)$ :** Using Eq. (5) from the main text:  $\Phi(1100) = \Phi_0 + \kappa \ln(1 + 1100) = 2.0 + (0.6994) \ln(1101)$ . Since  $\ln(1101) \approx 7.0039496$ ,  $\Phi(1100) \approx 2.0 + (0.6994 \times 7.0039496) \approx 2.0 + 4.898961 \approx 6.898961$ .

2. **Calculate terms in  $V[\Phi(1100)]$  using Eq. (2) and parameters:** (The formula for  $V[\Phi(z)]$  was displayed above)

- Term for  $\epsilon_1$ :  $\epsilon_1 e^{-\alpha_1 \Phi(1100)} = 0.60 \times e^{-(1.5 \times 6.898961)} \approx 1.92246 \times 10^{-5}$ .
- Term for  $\epsilon_2$ :  $\epsilon_2 e^{-\alpha_2 \Phi(1100)} = 0.47 \times e^{-(0.7 \times 6.898961)} \approx 0.0037562$ .
- Term for  $\epsilon_3$ :  $\epsilon_3 e^{-\lambda[\Phi(1100) - \phi_c]^2} = 0.60 \times e^{-0.28 \times (6.898961 - 7.6)^2} \approx 0.522863$ .
- Sum of terms inside the bracket:  $1 + (1.92246 \times 10^{-5}) + 0.0037562 + 0.522863 \approx 1.526638$ .

3. **Calculate  $V[\Phi(1100)]$ :**  $V[\Phi(1100)] = V_0 \times (\text{bracket value}) \approx (5.73 \times 10^{-44} \text{ kg m}^{-3}) \times 1.526638 \approx 8.7476 \times 10^{-44} \text{ kg m}^{-3}$ .

4. **Calculate  $\Lambda(1100)$ :** Using Eq. (3) from the main text:  $\Lambda(1100) = 8\pi G V[\Phi(1100)]$ .  $\Lambda(1100) \approx 8\pi \times (6.674 \times 10^{-11} \text{ m}^3 \text{ kg}^{-1} \text{ s}^{-2}) \times (8.7476 \times 10^{-44} \text{ kg m}^{-3}) \approx 1.4665 \times 10^{-52} \text{ s}^{-2}$ .

## Appendix C: Step-by-Step Calculation of the Hubble Parameter $H(z)$

This appendix demonstrates the calculation of the Hubble parameter  $H(z)$  using the benchmark parameters (Appendix A), the calculated  $\Lambda(z)$  (from Appendix B), and the Friedmann equation (Eq. (8) from the main text). The Friedmann equation is:

$$\begin{aligned} \frac{H(z)^2}{H_0^2} &= \Omega_{m0}(1+z)^3 + \Omega_{r0}(1+z)^4 + \Omega_{k0}(1+z)^2 \\ &\quad + \Omega_{\text{geom}0} \frac{\Lambda(z)}{\Lambda(0)}. \end{aligned} \quad (\text{C1})$$

For the benchmark model, the target  $H_0 \approx 69.5 \text{ km s}^{-1} \text{ Mpc}^{-1}$  (approximately  $2.252 \times 10^{-18} \text{ s}^{-1}$ ) is used. The benchmark derived density parameters at  $z = 0$  are:  $\Omega_{m0} \approx 0.24955$ ,  $\Omega_{k0} \approx 0.09735$ , and  $\Omega_{\text{geom}0} \approx 0.65301$ . For radiation, it is assumed a typical value  $\Omega_{r0} \approx 9.0 \times 10^{-5}$ . These values ensure the sum rule  $\Omega_{m0} + \Omega_{r0} + \Omega_{k0} + \Omega_{\text{geom}0} \approx 1.00000$ .

### 1. Calculation at $z = 0$

At  $z = 0$ ,  $\Lambda(z) = \Lambda(0)$ , so  $\Lambda(z)/\Lambda(0) = 1$ . Using Eq. (C1):

$$\begin{aligned} \frac{H(0)^2}{H_0^2} &= \Omega_{m0}(1)^3 + \Omega_{r0}(1)^4 + \Omega_{k0}(1)^2 + \Omega_{\text{geom}0}(1) \\ &= \Omega_{m0} + \Omega_{r0} + \Omega_{k0} + \Omega_{\text{geom}0} \\ &\approx 0.24955 + 0.00009 + 0.09735 + 0.65301 = 1.00000. \end{aligned}$$

So,  $H(0)^2 \approx H_0^2$ , which means  $H(0) \approx H_0 \approx 69.5 \text{ km s}^{-1} \text{ Mpc}^{-1}$ .

### 2. Calculation at $z = 1100$

#### 1. Values needed:

- $1 + z = 1101$ .
- $(1 + z)^2 = (1101)^2 = 1,212,201$ .
- $(1 + z)^3 = (1101)^3 \approx 1.334633 \times 10^9$ .
- $(1 + z)^4 = (1101)^4 \approx 1.469431 \times 10^{12}$ .
- From Appendix B,  $\Lambda(1100) \approx 1.4665 \times 10^{-52} \text{ s}^{-2}$ .
- From Appendix B,  $\Lambda(0) \approx 1.1010 \times 10^{-52} \text{ s}^{-2}$ .
- So,  $\frac{\Lambda(1100)}{\Lambda(0)} \approx \frac{1.4665}{1.1010} \approx 1.33197$ .

#### 2. Calculate each term in $E(z)^2 = H(z)^2/H_0^2$ using Eq. (C1):

- Matter term:  $\Omega_{m0}(1 + z)^3 \approx 0.24955 \times (1.334633 \times 10^9) \approx 3.33066 \times 10^8$ .

- Radiation term:  $\Omega_{r0}(1+z)^4 \approx (9.0 \times 10^{-5}) \times (1.469431 \times 10^{12}) \approx 1.32248 \times 10^8$ .
- Curvature term:  $\Omega_{k0}(1+z)^2 \approx 0.09735 \times (1.212201 \times 10^6) \approx 1.18000 \times 10^5$ .
- Geometric energy term:  $\Omega_{\text{geom}0} \frac{\Lambda(1100)}{\Lambda(0)} \approx 0.65301 \times 1.33197 \approx 0.86978$ .

### 3. Sum the terms to get $E(1100)^2$ :

$$\begin{aligned} E(1100)^2 &\approx (3.33066 \times 10^8) + (1.32248 \times 10^8) \\ &\quad + (1.18000 \times 10^5) + 0.86978 \\ &\approx 4.6543200086978 \times 10^8. \end{aligned}$$

(Note: The geometric energy and curvature terms are subdominant at this high redshift).

### 4. Calculate $H(1100)$ :

$$\begin{aligned} H(1100) &= H_0 \sqrt{E(1100)^2} \\ &\approx (69.5 \text{ km s}^{-1} \text{ Mpc}^{-1}) \times \sqrt{4.65432 \times 10^8} \\ &\approx (69.5 \text{ km s}^{-1} \text{ Mpc}^{-1}) \times 21573.873 \\ &\approx 1.499384 \times 10^6 \text{ km s}^{-1} \text{ Mpc}^{-1}. \end{aligned}$$

## Appendix D: Numerical Calculation of Cosmic Age

This appendix provides details on the numerical methods used to compute the cosmic age  $t_0$  presented in the main text, by evaluating the integral:

$$t_0 = \int_0^\infty \frac{dz}{(1+z)H(z)}, \quad (\text{D1})$$

where the Friedmann equation (Eq. (8) in the main text) gives  $H(z)$  as:

$$\begin{aligned} H(z) &= H_0 \left\{ \Omega_{m0}(1+z)^3 + \Omega_{r0}(1+z)^4 \right. \\ &\quad \left. + \Omega_{k0}(1+z)^2 + \Omega_{\text{geom}0} \frac{\Lambda(z)}{\Lambda(0)} \right\}^{1/2}. \end{aligned} \quad (\text{D2})$$

Due to the complexity of the term  $\Lambda(z)$ , which depends on  $\Phi(z)$  (Eq. (5) and Eq. (2)), this integral generally lacks a closed-form solution. The integral is evaluated numerically from  $z = 0$  to  $z_{\text{max}}$  (e.g.,  $z_{\text{max}} = 2000$ ).

### Method I: Composite Simpson's Rule

Define  $F(z) = 1/((1+z)H(z))$ . Discretize the interval  $[0, z_{\text{max}}]$  into  $N$  subintervals (with  $N$  even) of width  $h = z_{\text{max}}/N$ . Let  $z_i = i \cdot h$  for  $i = 0, \dots, N$ . Simpson's rule

gives:

$$\begin{aligned} t_0 &\approx \int_0^{z_{\text{max}}} F(z) dz \\ &\approx \frac{h}{3} \sum_{i=0}^N w_i F(z_i) \\ &= \frac{h}{3} [F(z_0) + 4F(z_1) + 2F(z_2) + \dots \\ &\quad + 4F(z_{N-1}) + F(z_N)], \end{aligned}$$

where the weights are  $w_i = \{1, 4, 2, 4, \dots, 2, 4, 1\}$ . The result  $t_0$  is obtained in units of  $1/H_0$  and then converted to Gyr.

### Method II: ODE Integration

Alternatively, solve the ordinary differential equation for lookback time  $t_L(z)$ :

$$\frac{dt_L}{dz} = \frac{1}{(1+z)H(z)}, \quad (\text{D3})$$

with  $t_L(0) = 0$ .

The age of the Universe is then  $t_0 = \lim_{z \rightarrow \infty} t_L(z)$ , approximated by  $t_L(z_{\text{max}})$ .

### Numerical Accuracy

Both methods yield consistent results. Numerical parameters were chosen to ensure the error in  $t_0$  is negligible (e.g., accuracy better than 0.01 Gyr).

## Appendix E: Calculation of the Effective Equation of State $w(z)$

This appendix details the calculation of the effective equation of state parameter  $w(z) = p_\Lambda(z)/\rho_\Lambda(z)$  for the geometric vacuum energy component, based on the model potential and the logarithmic evolution ansatz for the scalar field  $\Phi(z)$ .

Starting from the energy conservation equation for the geometric component,  $\dot{\rho}_\Lambda + 3H(\rho_\Lambda + p_\Lambda) = 0$ , and using the identification  $\rho_\Lambda(z) = V[\Phi(z)]$ , we derive the pressure as  $p_\Lambda(z) = -V[\Phi(z)] + \frac{\kappa V'[\Phi(z)]}{3}$ , where  $V' = dV/d\Phi$  and the logarithmic evolution ansatz (Eq. (5))  $\Phi(z) = \Phi_0 + \kappa \ln(1+z)$  has been assumed (leading to  $\dot{\Phi} = -\kappa H(z)$ ).

The equation of state parameter is therefore given by:

$$w(z) = \frac{p_\Lambda(z)}{\rho_\Lambda(z)} = -1 + \frac{\kappa V'[\Phi(z)]}{3V[\Phi(z)]}. \quad (\text{E1})$$

To calculate  $w(z)$ , we first need the derivative of the potential  $V(\Phi)$  given in Eq. (2):  $V(\Phi) =$

$V_0 \left[ 1 + \epsilon_1 e^{-\alpha_1 \Phi} + \epsilon_2 e^{-\alpha_2 \Phi} + \epsilon_3 e^{-\lambda(\Phi - \phi_c)^2} \right]$ . The derivative concerning  $\Phi$  is:

$$V'(\Phi) = V_0 \left[ -\alpha_1 \epsilon_1 e^{-\alpha_1 \Phi} - \alpha_2 \epsilon_2 e^{-\alpha_2 \Phi} - 2\lambda \epsilon_3 (\Phi - \phi_c) e^{-\lambda(\Phi - \phi_c)^2} \right]. \quad (\text{E2})$$

We use the benchmark parameters from Appendix A, including  $\kappa \approx 0.6994$ .

### 1. Step-by-Step Calculation Examples

#### a. Calculation at $z = 0$

1. **Calculate  $\Phi(0)$ :** As shown in Appendix B,  $\Phi(0) = \Phi_0 = 2.0$ .
2. **Calculate  $V(\Phi(0))$ :** As shown in Appendix B, the bracket value is  $\approx 1.145865$ .  $V(\Phi(0)) = V_0 \times (\text{bracket value})$ . We don't need the absolute value of  $V(0)$  and  $V'(0)$ , only their ratio multiplied by  $\kappa/3$ .

#### 3. Calculate terms in $V'(\Phi(0))$ using Eq. (E2):

- Term 1  $(-\alpha_1 \epsilon_1 e^{-\alpha_1 \Phi(0)})$ :  $-1.5 \times (0.60 \times e^{-3.0}) \approx -1.5 \times 0.02987224 \approx -0.044808$ .
- Term 2  $(-\alpha_2 \epsilon_2 e^{-\alpha_2 \Phi(0)})$ :  $-0.7 \times (0.47 \times e^{-1.4}) \approx -0.7 \times 0.11590057 \approx -0.081130$ .
- Term 3  $(-2\lambda \epsilon_3 (\Phi(0) - \phi_c) e^{-\lambda(\Phi(0) - \phi_c)^2})$ : We know  $(\Phi(0) - \phi_c) = -5.6$  and  $e^{-\lambda(\Phi(0) - \phi_c)^2} \approx 0.00015364$ . So,  $-2 \times 0.28 \times 0.60 \times (-5.6) \times 0.00015364 \approx +1.8816 \times 0.00015364 \approx +0.000289$ .
- Sum of terms inside  $V'(\Phi(0))$  bracket:  $-0.044808 - 0.081130 + 0.000289 \approx -0.125649$ .

So,  $V'(\Phi(0)) = V_0 \times (-0.125649)$ .

#### 4. Calculate the ratio term for $w(0)$ : $\frac{\kappa V'[\Phi(0)]}{3V[\Phi(0)]} = \frac{\kappa}{3} \times \frac{V_0 \times (-0.125649)}{V_0 \times (1.145865)} = \frac{0.6994}{3} \times \frac{-0.125649}{1.145865} \approx 0.23313 \times (-0.10965) \approx -0.02556$ .

#### 5. Calculate $w(0)$ using Eq. (E1): $w(0) = -1 + \frac{\kappa V'[\Phi(0)]}{3V[\Phi(0)]} \approx -1 + (-0.02556) \approx -1.02556$ .

So, for the benchmark parameters, the effective equation of state at  $z = 0$  is slightly phantom ( $w < -1$ ).

#### b. Calculation at $z = 1$

1. **Calculate  $\Phi(1)$ :**  $\Phi(1) = \Phi_0 + \kappa \ln(1 + 1) = 2.0 + 0.6994 \ln(2)$ .  $\ln(2) \approx 0.69315$ .  $\Phi(1) \approx 2.0 + (0.6994 \times 0.69315) \approx 2.0 + 0.48481 \approx 2.48481$ .

### 2. Calculate terms in $V[\Phi(1)]$ using Eq. (2):

- Term 1:  $0.60 \times e^{-1.5 \times 2.48481} = 0.60 \times e^{-3.7272} \approx 0.60 \times 0.02406 \approx 0.014436$ .
- Term 2:  $0.47 \times e^{-0.7 \times 2.48481} = 0.47 \times e^{-1.7394} \approx 0.47 \times 0.17563 \approx 0.082546$ .
- Term 3: Exponent  $= -0.28 \times (2.48481 - 7.6)^2 = -0.28 \times (-5.11519)^2 \approx -0.28 \times 26.165 \approx -7.3262$ .  $0.60 \times e^{-7.3262} \approx 0.60 \times 0.000658 \approx 0.000395$ .
- Bracket value:  $1 + 0.014436 + 0.082546 + 0.000395 \approx 1.097377$ .

$$V(\Phi(1)) = V_0 \times (1.097377).$$

### 3. Calculate terms in $V'(\Phi(1))$ using Eq. (E2):

- Term 1:  $-1.5 \times (0.014436) \approx -0.021654$ . (Using Term 1 value from  $V(\Phi(1))$  calculation above)
- Term 2:  $-0.7 \times (0.082546) \approx -0.057782$ . (Using Term 2 value)
- Term 3:  $(\Phi(1) - \phi_c) = -5.11519$ .  $-2 \times 0.28 \times 0.60 \times (-5.11519) \times e^{-7.3262} \approx +1.7186 \times 0.000658 \approx +0.001131$ .
- Sum of terms inside  $V'(\Phi(1))$  bracket:  $-0.021654 - 0.057782 + 0.001131 \approx -0.078305$ .

$$V'(\Phi(1)) = V_0 \times (-0.078305).$$

#### 4. Calculate the ratio term for $w(1)$ : $\frac{\kappa V'[\Phi(1)]}{3V[\Phi(1)]} = \frac{0.6994}{3} \times \frac{V_0 \times (-0.078305)}{V_0 \times (1.097377)} \approx 0.23313 \times (-0.071356) \approx -0.01663$ .

#### 5. Calculate $w(1)$ using Eq. (E1): $w(1) = -1 + \frac{\kappa V'[\Phi(1)]}{3V[\Phi(1)]} \approx -1 + (-0.01663) \approx -1.01663$ .

The equation of state is still slightly phantom at  $z = 1$ .

## 2. Summary and Discussion

The calculation shows that for the benchmark parameters derived from fitting  $H(z)$  data (which favors  $\Omega_k > 0$ ), the effective equation of state  $w(z)$  derived from the logarithmic evolution ansatz is slightly phantom ( $w < -1$ ) at low redshifts ( $z = 0, z = 1$ ). This is an interesting feature that could be compared with detailed constraints on  $w(z)$  from SNe Ia and BAO data. A plot of  $w(z)$  over a wider range of redshifts could be generated using this method. It is also important to check how solving the full equation of motion (Eq. (7)) instead of using the ansatz (Eq. (5)) might affect the calculated  $w(z)$ .



## Appendix F: Numerical Solution of Full Field Dynamics and Comparison with Ansatz

To assess the validity and accuracy of the logarithmic evolution ansatz for the scalar field  $\Phi(z)$  (Eq. (5) in the main text), we solved the full system of coupled cosmological equations numerically. This involves simultaneously integrating the Friedmann equation (Eq. (8)) and the scalar field equation of motion (Eq. (7)).

### Methodology

The system was converted into a set of first-order ordinary differential equations (ODEs) using  $N = \ln a$  as the independent variable, with state vector  $Y = [\Phi, \Psi]$  where  $\Psi = d\Phi/dN$ . The equations solved are those derived in standard cosmological perturbation theory adapted for this potential  $V(\Phi)$  (Eq. (2)). Specifically, we solve:

$$\begin{aligned}\frac{d\Phi}{dN} &= \Psi \\ \frac{d\Psi}{dN} &= -\left(3 + \frac{1}{2E^2} \frac{d(E^2)}{dN}\right) \Psi - \frac{V'(\Phi)}{H_0^2 E^2}\end{aligned}$$

where  $E^2(N, \Phi) = H^2/H_0^2$  is given by the right-hand side of Eq. (8) (with  $\Omega_{\text{geom}}(z)$  replaced by  $\Omega_{\text{geom}0}V[\Phi(z)]/V[\Phi_0]$ ), and  $V'(\Phi) = dV/d\Phi$  is derived from Eq. (2).

Given the focus on late-time cosmology and the benchmark model derived from fitting low-redshift data, we chose to integrate the system *backwards* in  $N$  starting from the present day ( $N = 0, z = 0$ ) up to  $N \approx -7$  (corresponding to  $z \approx 1100$ ). The initial conditions at  $N = 0$  were set to match the benchmark model and the logarithmic ansatz at this point:

- $\Phi(N = 0) = \Phi_0 = 2.0$  (from Appendix A).
- $\Psi(N = 0) = d\Phi/dN|_{N=0}$ . Using the ansatz  $\Phi \approx \Phi_0 - \kappa N$  (since  $N = \ln a = -\ln(1+z)$  for  $a_0 = 1$ ),

we have  $d\Phi/dN = -\kappa$ . Thus, we set  $\Psi(0) = -\kappa \approx -0.6994$ . This is consistent with  $\dot{\Phi} = -\kappa H$ , which leads to  $\Psi = \dot{\Phi}/H = -\kappa$ .

The ODE system was solved using a standard Runge-Kutta method (specifically `scipy.integrate.solve_ivp` with RK45) with appropriate tolerance settings.

### Results and Comparison

The results of the numerical integration are compared with the predictions from the logarithmic evolution ansatz in Figure 4.

The key findings from this comparison are:

1. The logarithmic evolution ansatz (Eq. (5)) provides an excellent approximation (better than 1).
2. The effective equation of state parameter  $w(z)$  shows more significant differences. The full numerical solution suggests a rapid transition towards  $w \approx +1$  (stiff fluid-like behavior) at  $z \gtrsim 1$ , differing considerably from the slower evolution predicted by directly applying the ansatz formula for  $w(z)$ . This highlights that while the background evolution is well-approximated, the detailed physical interpretation of the geometric energy component's nature (via  $w(z)$ ) is more sensitive to the full dynamics.
3. The numerical solution remained stable despite the potential having a tachyonic region ( $V'' < 0$ ) at higher redshifts (Appendix B). This might indicate that the field trajectory, under these specific initial conditions, crosses the unstable region rapidly without significant deviation from the overall path dictated by the stable parts of the potential and cosmic friction.

A more detailed investigation of the equation of state and the impact of initial conditions requires further study beyond the scope of this appendix.

- 
- [1] A. Einstein, Sitzungsber. Preuss. Akad. Wiss. **1917**, 142 (1917).
  - [2] E. P. Hubble, Proc. Natl. Acad. Sci. USA **15**, 168 (1929).
  - [3] Y. B. Zeldovich, Sov. Phys. Usp. **11**, 381 (1968).
  - [4] S. Weinberg, Rev. Mod. Phys. **61**, 1 (1989).
  - [5] J. Martin, *Comptes Rendus Physique* **13**, 566 (2012).
  - [6] V. Sahni and A. Starobinsky, *Int. J. Mod. Phys. D* **9**, 373 (2000).
  - [7] J. P. Ostriker and P. J. Steinhardt, *Nature* **377**, 600 (1995).
  - [8] A. G. Riess *et al.*, *Astron. J.* **116**, 1009 (1998).
  - [9] S. Perlmutter *et al.*, *Astrophys. J.* **517**, 565 (1999).
  - [10] P. de Bernardis *et al.*, *Nature* **404**, 955 (2000).
  - [11] Planck Collaboration, N. Aghanim, Y. Akrami, M. Ashdown, J. Aumont, C. Baccigalupi, M. Ballardini, A. J. Banday, R. B. Barreiro, N. Bartolo, *et al.*, *Astron. Astrophys.* **641**, A6 (2020), [arXiv:1807.06209 \[astro-ph.CO\]](#).
  - [12] C. Vafa, (2005), [arXiv:hep-th/0509212 \[hep-th\]](#).
  - [13] G. Obied, H. Ooguri, L. Spodyneiko, and C. Vafa, (2018), [arXiv:1806.08362 \[hep-th\]](#).
  - [14] A. G. Riess, S. Casertano, W. Yuan, L. M. Macri, and D. Scolnic, *Astrophys. J.* **876**, 85 (2019).
  - [15] A. G. Riess, W. Yuan, L. M. Macri, D. Scolnic, D. Brout, S. Casertano, D. O. Jones, Y. Murakami, L. Breuval, T. G. Brink, *et al.*, *Astrophys. J. Lett.* **934**, L7 (2022), [arXiv:2112.04510 \[astro-ph.CO\]](#).
  - [16] V. Poulin, T. L. Smith, T. Karwal, and M. Kamionkowski, *Phys. Rev. Lett.* **122**, 221301 (2019).
  - [17] T. Karwal and M. Kamionkowski, *Phys. Rev. D* **94**, 103523 (2016).

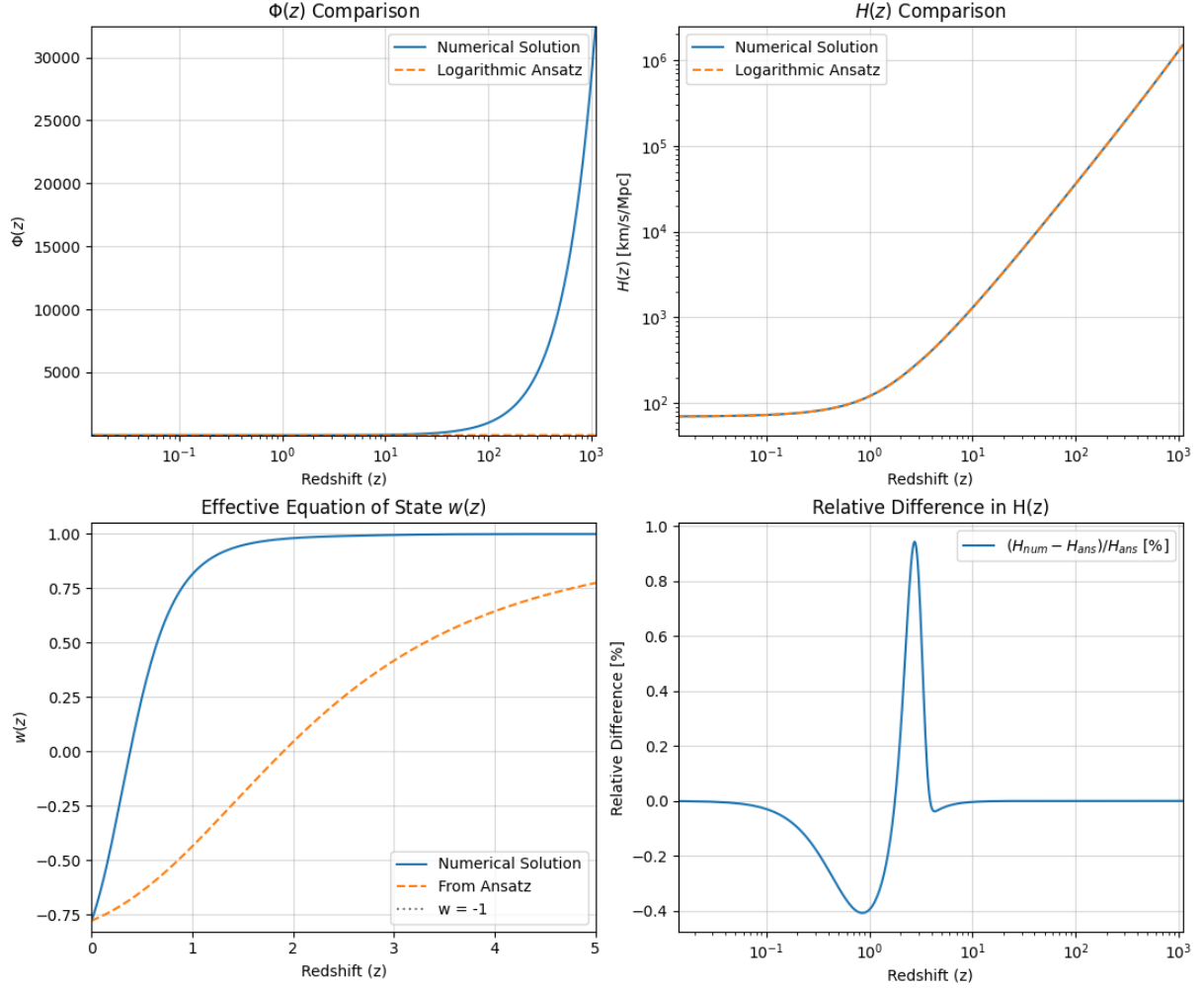


FIG. 4. Comparison between the numerical solution of the full equations of motion (solid blue lines) and the logarithmic evolution ansatz (dashed orange lines) for the benchmark model parameters (Appendix A). **Top Left:** Evolution of the scalar field  $\Phi(z)$ . The two solutions are virtually indistinguishable. **Top Right:** Evolution of the Hubble parameter  $H(z)$  (log-log scale). Again, the agreement is excellent. **Bottom Left:** Effective equation of state parameter  $w(z)$ . While both solutions start near  $w \approx -1.026$  at  $z = 0$ , the numerical solution rapidly evolves towards  $w \approx +1$  for  $z \gtrsim 1$ , whereas the ansatz predicts a slower evolution. **Bottom Right:** Relative percentage difference between the numerical  $H(z)$  and the ansatz  $H(z)$ . The difference remains below 1% across the plotted redshift range, peaking near  $z \approx 1$ .

- [18] B. S. Acharya, Adv. Theor. Math. Phys. **3**, 227 (1999), [arXiv:hep-th/0011089 \[hep-th\]](#).
- [19] K. Becker, M. Becker, and J. H. Schwarz, *String Theory and M-Theory: A Modern Introduction* (Cambridge University Press, Cambridge, 2007).
- [20] I. Zlatev, L. Wang, and P. J. Steinhardt, Phys. Rev. Lett. **82**, 896 (1999).
- [21] B. S. Acharya, Int. J. Mod. Phys. A **34**, 1943003 (2019).
- [22] P. J. Steinhardt and N. Turok, Science **296**, 1436 (2002).
- [23] L. Baum and P. H. Frampton, Mod. Phys. Lett. A **25**.
- [24] D. D. Joyce, Journal of Differential Geometry **43**, 291 (1996).
- [25] D. D. Joyce, *Compact Manifolds with Special Holonomy* (Oxford University Press, Oxford, 2000).
- [26] A. Kovalev, Journal für die reine und angewandte Mathematik (Crelle's Journal) **565**, 125 (2003).
- [27] A. Corti, M. Haskins, J. Nordström, and T. Pacini, Duke Mathematical Journal **164**, 1971 (2015), [arXiv:1207.4470 \[math.DG\]](#).
- [28] F. Beutler, C. Blake, M. Colless, D. H. Jones, L. Staveley-Smith, L. Campbell, Q. Parker, W. Saunders, and F. Watson, Monthly Notices of the Royal Astronomical Society **416**, 3017 (2011).
- [29] A. J. Ross, L. Samushia, C. Howlett, W. J. Percival, A. Burden, and M. Manera, Monthly Notices of the Royal Astronomical Society **449**, 835 (2015).
- [30] S. Alam, M. Ata, S. Bailey, F. Beutler, D. Bizyaev, J. A. Blazek, A. S. Bolton, J. R. Brownstein, A. Burden, C. H. Chuang, and others (BOSS Collaboration), Mon. Not. Roy. Astron. Soc. **470**, 2617 (2017), [arXiv:1607.03155 \[astro-ph.CO\]](#).
- [31] D. M. Scolnic, D. O. Jones, A. Rest, Y. C. Pan, R. Chornock, R. J. Foley, M. E. Huber, R. Kessler, G. Narayan, A. G. Riess, et al., Astrophys. J. **859**, 101

- (2018), [arXiv:1710.00845 \[astro-ph.CO\]](#).
- [32] T. M. C. Abbott and others (DES Collaboration), *Phys. Rev. D* **98**, 043526 (2018), [arXiv:1708.01530 \[astro-ph.CO\]](#).
  - [33] H. Hildebrandt, M. Viola, C. Heymans, S. Joudaki, K. Kuijken, C. Blake, T. Erben, B. Joachimi, D. Klaes, L. Miller, and others (KiDS Collaboration), *Mon. Not. Roy. Astron. Soc.* **465**, 1454 (2017), [arXiv:1606.05338 \[astro-ph.CO\]](#).
  - [34] D. Foreman-Mackey, D. W. Hogg, D. Lang, and J. Goodman, *Publ. Astron. Soc. Pac.* **125**, 306 (2013), [arXiv:1202.3665 \[astro-ph.IM\]](#).
  - [35] A. Gelman and D. B. Rubin, *Statistical Science* **7**, 457 (1992).
  - [36] H. Akaike, *IEEE Transactions on Automatic Control* **AC-19**, 716 (1974).
  - [37] G. E. Schwarz, *Annals of Statistics* **6**, 461 (1978).
  - [38] R. E. Kass and A. E. Raftery, *Journal of the American Statistical Association* **90**, 773 (1995).
  - [39] G. E. Addison, D. J. Watts, C. L. Bennett, M. Halpern, G. Hinshaw, and J. L. Weiland, *Astrophys. J.* **818**, 132 (2016), [arXiv:1511.00055 \[astro-ph.CO\]](#).